Review article

Seyyed Ali Hassani Gangaraj and Francesco Monticone*

Molding light with metasurfaces: from far-field to near-field interactions

https://doi.org/10.1515/nanoph-2017-0126
Received December 15, 2017; revised March 16, 2018; accepted March 30, 2018

Abstract: The field of metasurfaces is revolutionizing the way we control and manipulate light and electromagnetic fields based on engineered ultrathin structures. In this review article, we discuss the theory, modeling, and applications of metasurfaces, with particular focus on controlling the near-field response of sources close to the artificial surface. Although metasurfaces have attracted large attention for their ability to control and mold the wavefront of propagating waves, hence acting as flat lenses, they can also be used to modify the emission/radiation from near-field sources and control the generation and propagation of surface waves guided and confined along the surface. We discuss the analytical modeling of metasurfaces treated as homogenized impedance sheets and elucidate the application and limits of this approach for near-field sources. We devote a large part of the review article to anisotropic and hyperbolic metasurfaces, which enable some of the most exciting and extreme examples of anomalous surface-wave propagation on planarized artificial structures, with important implications for light focusing, confinement, and subwavelength imaging. We also connect these ideas with the emerging area of 2D materials and discuss how to implement hyperbolic metasurfaces with graphene and black phosphorus. We hope that this review article may provide the reader with relevant physical insights and useful analytical tools to study metasurfaces and their near-field interactions with localized sources and, more generally, offer an overview of this field and its ambitious goal of ideal light control on a surface.

Keywords: 2D materials; metamaterials; metasurfaces; nanophotonics; surface waves.

***Corresponding author: Francesco Monticone,** School of Electrical and Computer Engineering, Cornell University, Ithaca, NY 14853, USA, e-mail: francesco.monticone@cornell.edu
Seyyed Ali Hassani Gangaraj: School of Electrical and Computer Engineering, Cornell University, Ithaca, USA

1 Introduction

The beginning of the 21st century has seen a growing interest in engineered artificial materials and structures with unusual electromagnetic and optical properties. Advances in the fields of metamaterials, photonic crystals, nanophotonics, and metal optics have largely extended the range of possibilities available in applied electromagnetics and photonics, beyond what is achievable with naturally occurring materials and conventional optical structures [1, 2]. Among these different areas, the concept of "metasurfaces" – the planarized version of metamaterials – has emerged as one of the most promising research directions from both fundamental and practical standpoints.

The modern field of metasurfaces builds upon earlier investigations on artificial surfaces, reflect- and transmitarrays at microwaves (e.g. [3, 4]), as well as planar periodic structures at optical frequencies, such as planar gratings (e.g. [5–7]). However, modern metasurfaces are drastically distinct from these earlier examples of artificial planar structures for a number of reasons, making the field of metasurfaces a new and exciting area of science and technology. For example, historically, artificial surfaces at microwave frequencies have been designed by periodically patterning thin metallic layers to realize so-called "frequency-selective surfaces" (FSSs) [4]. FSSs act as frequency filters for propagating waves, and their frequency-selective response originates from their periodicity comparable to the wavelength, which determines the allowed and forbidden frequency bands [4], similar to the modern concept of photonic crystals. Conversely, modern metasurfaces typically have periodicity much smaller than the wavelength and are therefore more similar to metamaterials, which can be homogenized in terms of average fields and effective macroscopic properties. As in 3D metamaterials, the unusual properties of metasurfaces arise from their resonant inclusions acting as artificial meta-atoms and not, or not only, from their periodicity.

Many seminal contributions have helped establish the modern field of metasurfaces. Among several relevant papers, we would like to mention the theoretical works of

Edward F. Kuester and Christopher L. Holloway [8–12] and Sergei Tretyakov [13], which have established the theoretical framework to study metasurfaces as homogenized planar sheets with effective properties, and the works of Federico Capasso [14, 15], which have experimentally demonstrated the ability to control the reflection and transmission of light impinging on a metasurface based on "generalized laws of reflection and refraction" that originate from the inhomogeneous phase profile imparted by the metasurface. In many ways, Capasso's demonstration of an optical metasurface in 2011 [14] represented the "tipping point" of the field of metasurfaces, as it proved the feasibility of the ambitious vision of replacing thick and bulky optical elements with ultrathin engineered surfaces, for light focusing, anomalous reflection/refraction, wavefront shaping, holography, etc. Other notable works have then studied the limits of metasurface efficiency [16, 17] and have introduced new designs that improve the ability to control the transmitted or reflected light with almost ideal efficiency and unprecedented flexibility [18–26].

Despite its relatively young history, many review papers and book chapters have been written on the field of electromagnetic and optical metasurfaces and their many applications in different frequency ranges, spanning from novel antenna designs to flat optical lenses [27–30]. Most of these papers focus on the response of metasurfaces illuminated by propagating plane waves or, more generally, fields that originate far from the surface (several wavelengths away; i.e. in the "far-field"), with the goal of tailoring the transmitted or reflected wavefront at will. In the present review article, instead, we focus on the response of metasurfaces excited by sources in the "near-field", for example, a point dipole placed near the surface, which may model a short antenna, or a localized quantum emitter. This problem is qualitatively different from the far-field problem for several reasons and involves relevant physical effects that are not discussed in most papers dedicated to metasurfaces. Notably, a near-field source may excite the "surface modes" of the artificial surface, which can be exploited and engineered to confine and guide electromagnetic fields in specific directions along the metasurface. Metasurfaces may therefore be used to control the emission/radiation of localized sources and guide the radiated energy along the planar structure in the form of surface waves with tailored propagation and radiation properties. Figure 1 illustrates this general vision of near-field light control on engineered surfaces. Furthermore, even the analytical modeling of metasurfaces excited in the near-field requires different and specific considerations compared to the conventional far-field

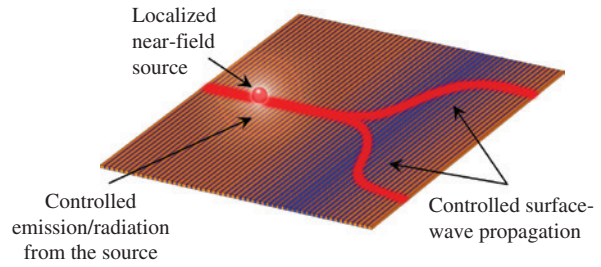

Figure 1: Illustration of an engineered metasurface illuminated by a source in the near-field.
In this illustration, a strongly anisotropic metasurface composed of strips of different materials is used to control the emission from a localized source in the near-field and guide the resulting surface waves in desired directions along the surface.

case. For example, particular care should be taken to ensure that the homogenization process is accurate even from the point of view of sources and observation points very close to the metasurfaces, as will be discussed in the following.

We also would like to highlight that, in the general context of applied electromagnetics, engineering the radiation of a source in proximity to a metasurface is essentially the same task as designing a leaky-wave antenna, a well-studied problem in the microwave and antenna communities [31, 32]. In this scenario, the near fields of an electrically small antenna (e.g. a cap-loaded short dipole at microwaves) can be transformed into guided surface waves, which propagate along the surface and may gradually lose energy due to material absorption, or leaky-wave radiation into free space [33, 34]. Indeed, the antenna community has investigated and proposed several strategies to control and tune the propagation and leakage properties of surface waves using, for example, modulated metasurfaces or transformation-optics techniques [35–40]. Therefore, the concepts and methods discussed in this review article, while being focused on nanophotonic structures and applications, also apply to metasurfaces at microwave frequencies. In addition, many of the analytical modeling techniques discussed here are indeed directly borrowed from microwave and antenna theory.

Within this context, in this review article, we first discuss the general theory and analytical modeling of metasurfaces, with particular emphasis on their interactions with localized near-field sources, and we then concentrate on a specific class of metasurfaces, namely, anisotropic and hyperbolic metasurfaces, which are of particular interest for their ability to control and guide the surface waves in anomalous and extreme ways, with important implications for several practical applications. Finally, we also discuss the connection of these ideas

with emerging 2D materials, such as graphene and black phosphorus (BP).

2 Theory: analytical modeling, homogenization conditions, and limits

In this section, we review the general theory and analytical modeling of metasurfaces, which can be applied to either far-field or near-field excitations, with the goal to provide the reader with the necessary analytical tools to study these problems in different scenarios.

In general, the analysis of the interaction between a point source and a metasurface requires considerable computational effort due to the complex nature of the interaction, which includes the combined effects of free-space radiation and excitation of guided modes. In this context, conventional full-wave numerical simulators, based, for example, on finite-element or finite-difference methods, cannot directly be used to solve the problem of a periodic surface with a single nonperiodic source, as the application of periodic boundary conditions would simply lead to the infinite periodic replication of the point source. The easiest approach to overcome this issue is to consider a finite, yet sufficiently large, structure, with a large number of periods, and a single nonperiodic source; however, this approach has several drawbacks, especially because it is very computationally demanding and time-consuming. Furthermore, it was shown in Ref. [8] that finite-thickness effective-medium models of metasurfaces, in terms of effective material properties as for 3D metamaterials, are typically inappropriate and ineffective. Instead, metasurfaces are more correctly modeled as 2D surfaces in terms of homogenized effective surface conductivities or surface impedances [13, 41–46] (or equivalent electric and magnetic susceptibility tensors [9–12]), as discussed in the following.

As usually done, the electromagnetic boundary conditions between two regions of space can be expressed as a set of equations for the normal and tangential components of the electric/magnetic fields on the two sides of the boundary. For the tangential components, we have

$$\begin{aligned} +\hat{\mathbf{z}}\times(\mathrm{H}^1-\mathrm{H}^2)&=\mathrm{J}_e^s \\ -\hat{\mathbf{z}}\times(\mathrm{E}^1-\mathrm{E}^2)&=\mathrm{J}_m^s \end{aligned} \tag{1}$$

which indicate that an arbitrary jump in the tangential component of the fields requires the presence of electric and magnetic surface currents, J_e^s and J_m^s ($\hat{\mathbf{z}}$ is the normal direction to the interface). The boundary conditions for the normal components are automatically satisfied if the conditions on the tangential components are satisfied. Within this framework, the original problem of a generic metasurface in a host medium or host structure, as shown in Figure 2, can be modeled as an electric conductivity tensor $\underline{\boldsymbol{\sigma}}_e$ and a magnetic conductivity tensor $\underline{\boldsymbol{\sigma}}_m$, relating the currents induced on the metasurface to the local tangential component of the fields. At this point, one has to distinguish between two general cases of interest: (i) Penetrable metasurfaces, namely, metasurfaces allowing nonzero fields at both sides (as in the case of metasurfaces used as flat lenses and transmit arrays). In this case, for metasurfaces with no magnetoelectric coupling, the current on the metasurface should be calculated from the "average" of the fields at the two sides of the metasurface, namely, $\mathrm{J}_e^s=\underline{\boldsymbol{\sigma}}_e\cdot\mathrm{E}_\mathrm{T}^{\mathrm{avg}}$ and $\mathrm{J}_m^s=\underline{\boldsymbol{\sigma}}_\mathrm{m}\cdot\mathrm{H}_\mathrm{T}^{\mathrm{avg}}$, where $\mathrm{E}_\mathrm{T}^{\mathrm{avg}}=\frac{1}{2}(\mathrm{E}_\mathrm{T}^1+\mathrm{E}_\mathrm{T}^2)$ and $\mathrm{H}_\mathrm{T}^{\mathrm{avg}}=\frac{1}{2}(\mathrm{H}_\mathrm{T}^1+\mathrm{H}_\mathrm{T}^2)$ are the average tangential fields on the surface [47, 48]. Instead, in the most general case of metasurfaces with magnetoelectric coupling (bianisotropy), it is generally not possible to calculate the induced electric and magnetic currents from

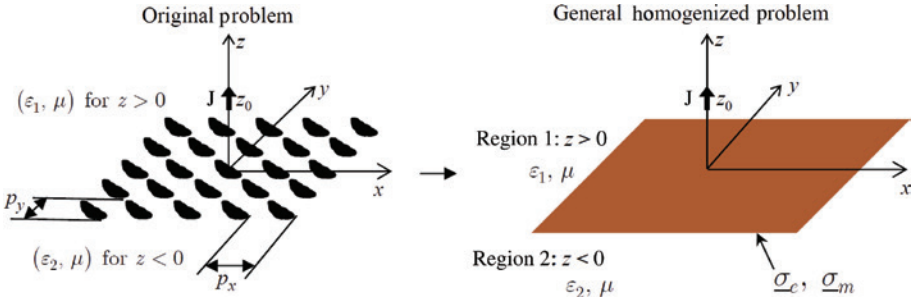

Figure 2: Analytical modeling of metasurfaces.
Original problem of a planar array of meta-atoms in a host medium/structure (left) and the corresponding equivalent homogenized problem (right) represented as a generic sheet with electric conductivity tensor $\underline{\boldsymbol{\sigma}}_e$ and magnetic conductivity tensor $\underline{\boldsymbol{\sigma}}_m$. Adapted with permission from Ref. [46].

the average fields, as these average values do not have a well-defined physical meaning due to the magnetoelectric coupling [29, 48]. In this case, one should calculate the induced currents from the "incident" fields through a 6×6 admittance matrix, which corresponds to an equivalent T-circuit [29]. (ii) Impenetrable metasurfaces, where the fields exist only at one side of the metasurface (as in the case of metasurfaces realized by patterning/modulating a metallic ground plane). In this case, Eq. (1) reduces to $\hat{\mathbf{z}}\times\mathrm{H}^1=\mathrm{J}_e^s=\underline{\boldsymbol{\sigma}}_e\cdot\mathrm{E}_\mathrm{T}^1$ and $-\hat{\mathbf{z}}\times\mathrm{E}^1=\mathrm{J}_m^s=\underline{\boldsymbol{\sigma}}_m\cdot\mathrm{H}_\mathrm{T}^1$, which relate the tangential component of the fields on the same side through the electric or magnetic surface conductivity (in this case, the currents are not proportional to the averaged fields at the two sides of the metasurface). We will further discuss the difference between penetrable and impenetrable metasurfaces and their modeling in terms of two- and one-sided surface impedances in Section 2.2.

In the case of a penetrable metasurface between two half-spaces, as in Figure 2, the electric field E^n, in each region $n=1$, 2, generated by a generic current source J above the metasurface, can be obtained as

$$\mathrm{E}^n=-j\omega\mu\int_\Omega\underline{\mathrm{G}}_e^n(\mathrm{r},\mathrm{r}')\cdot\mathrm{J}(\mathrm{r}')d\Omega' \tag{2}$$

where μ is the magnetic permeability of the surrounding medium and $\underline{\mathrm{G}}_e^n$ is the "electric homogenized dyadic Green's function" representing the electromagnetic response at any point r, in region $n=1$, 2, to an arbitrary polarized point source at a specific location r′ (here and throughout the review article, we assume harmonic fields with time convention $e^{j\omega t}$). In other words, the dyadic Green's function represents the (vectorial) electromagnetic spatial impulse response of the system. Next, considering a source in region 1, the corresponding Green's function in this region can be decomposed in "free-space" Green's function (namely, the Green's function in the absence of the metasurface) and "scattered/reflected" Green's function (i.e. $\underline{\mathrm{G}}_e^1=\underline{\mathrm{G}}_0^1+\underline{\mathrm{G}}_r^1$). For the second region, beyond the metasurface, only the "transmitted" Green's function is necessary, $\underline{\mathrm{G}}_e^2=\underline{\mathrm{G}}_t^2$. As usually done, reflected and transmitted Green's functions can be written in an angular spectrum representation (namely, a plane-wave expansion), which takes the general form [49–51]

$$\begin{aligned}\underline{\mathrm{G}}_r^1(\mathrm{r},\mathrm{r}')&=\frac{j}{8\pi^2}\iint\frac{1}{k_{1z}}\underline{\mathrm{M}}_r e^{j\mathrm{k}_1^+\cdot\mathrm{r}}e^{-j\mathrm{k}_1^-\cdot\mathrm{r}'}dk_x dk_y\\ \underline{\mathrm{G}}_t^2(\mathrm{r},\mathrm{r}')&=\frac{j}{8\pi^2}\iint\frac{1}{k_{1z}}\underline{\mathrm{M}}_t e^{j\mathrm{k}_2^-\cdot\mathrm{r}}e^{-j\mathrm{k}_1^-\cdot\mathrm{r}'}dk_x dk_y\end{aligned} \tag{3}$$

where $\mathrm{k}_n^\pm=\hat{\mathrm{x}}k_x+\hat{\mathrm{y}}k_y\pm\hat{\mathrm{z}}k_{nz}$ is the total wavevector in each region, $k_{nz}=\sqrt{k_n^2-k_x^2-k_y^2}$ is the normal wavenumber, and $\underline{\mathrm{M}}_r$ and $\underline{\mathrm{M}}_t$ are matrices that depend on the reflection and transmission coefficients for s- and p-polarized fields [for s-polarization or transverse-electric (TE) polarization, the electric field is parallel to the interface, whereas, for p-polarization or transverse-magnetic (TM) polarization, the magnetic field is parallel to the interface]. These coefficients can be determined by imposing the boundary conditions (1) and, for simple cases, they are given in the literature (see Ref. [46]). The integrand of Eq. (3) may diverge at the poles of the reflection/transmission coefficients. These singularities are associated with the eigenmodes of the structure (i.e. the solutions of the source-free wave equation) and correspond, in our case, to the surface modes of the metasurface. In general, these guided modes are classified as (i) "bound surface waves" (e.g. surface plasmon polaritons) with purely imaginary out-of-plane wavenumber k_z, which indicates the degree of confinement of the mode to the surface, and (ii) "leaky surface waves", with complex out-of-plane wavenumber k_z, indicating confinement *and* radiation leakage as the wave propagates along the surface. We refer the reader to Refs. [31, 47] for an in-depth discussion of bound and leaky waves in different planar geometries and Refs. [32, 52] for other, more exotic effects such as the existence of trapped states known as bound states in the continuum, or embedded eigenstates, in planar gratings and artificial surfaces.

For a given metasurface and excitation, the theoretical formulation above allows determining the electromagnetic fields everywhere if the electric and magnetic conductivity tensors that model the metasurface are available. Several methods have been proposed in the literature to determine the tensors $\underline{\boldsymbol{\sigma}}_m$ and $\underline{\boldsymbol{\sigma}}_e$ either in terms of electric and magnetic susceptibilities [8, 9, 12, 47, 50] (susceptibilities are related to the electric and magnetic polarizability densities of the scatterers per unit area) or surface impedances and admittances [41, 42]. The properties of the elements composing the metasurface determine which method is easier to apply [46]. For example, for a simple metasurface composed of metal patches, the susceptibilities are available in Refs. [50, 53] and the surface impedance values are available in Refs. [41, 42], whereas, for more complex periodic elements, Holloway et al. in Ref. [47] provide a method for finding the susceptibilities from numerical computations.

2.1 Accuracy of metasurface homogenization

As mentioned in Section 1, the analysis of near-field interactions between a source and a metasurface requires to

pay particular attention to the validity of the metasurface homogenization. In this section, we would like to provide the reader with qualitative insight into the accuracy of this modeling approach.

The "characteristic lengths" involved in the problem under consideration are the spatial periods of the metasurface elements p_x and p_y (see Figure 2), the wavelength in the surrounding medium λ_1, the distance of the source from the metasurface z_0, and the distance of an observation point z. In particular, the latter two parameters play a crucial role in the validity of the homogenization approach for a source/observation in the near field of the metasurface, whereas only the metasurface period relative to the incident wavelength is important in the case of a conventional metasurface problem with far-field illumination and observation point. The "first homogenization condition" requires that the incident field radiated by the point source should vary little over one spatial period of the metasurface along the x- and y-directions [42]. The field radiated by an ideal point source can be represented as a continuous plane-wave spectrum containing (i) propagating waves with transverse (in-plane) wavenumber $k_T=\sqrt{k_x^2+k_y^2}\le|k_1|$ and (ii) evanescent waves with $k_T=\sqrt{k_x^2+k_y^2}>|k_1|$. While all propagating waves satisfy the first homogenization condition for a metasurface with $p\ll\lambda_1$ where $p=\mathrm{Max}(p_x, p_y)$, the situation is a bit trickier for the evanescent portion of the spectrum. First, if a surface mode is excited on the metasurface with wavenumber k_{SW}, it is necessary that the surface-mode wavelength is larger than the metasurface period: $p\ll\lambda_{SW}=2\pi/k_{SW}$. This limit, combined with the fact that surface waves with larger in-plane wavenumber k_{SW} decay faster in the out-of-plane direction, allows setting an approximate lower bound on the distance of the source from the surface. In fact, for a sufficiently distant point source, the evanescent waves with transverse wavenumber large enough to "see" the periodicity of the metasurface may completely decay before even reaching the metasurface. Based on numerical experiments, it was found in Ref. [42] that these considerations lead to an approximate lower bound for the source distance above the surface that reads: $z_0>p$.

The "second homogenization condition" requires that the evanescent field scattered by the metasurface should be negligible at the observation point. Assuming that the first condition is satisfied, the field scattered by the metasurface admits a Bloch-Floquet representation in which all higher-order space harmonics are evanescent. In this case, the second condition is satisfied if the space harmonic with smallest attenuation constant in the orthogonal z-direction has negligible amplitude at the observation point. In Ref. [42], it was found that the attenuation of this space harmonic can be approximated as $\alpha_z\simeq 2\pi/p$. Based on additional considerations motivated by numerical experiments, an approximate lower bound for the observation point can then be set as $z>p$ [42]. If both homogenization conditions are met, an analytical model based on effective conductivity tensors and homogenized Green's function is accurate and can be used to predict the near-field interaction of a point source with an arbitrary metasurface.

2.2 Metasurfaces as surface-impedance sheets, and limits on wavefront shaping

To complete our theoretical discussion, in this section, we briefly present two intuitive models of a metasurface in terms of surface-impedance sheets (see Figure 3) and discuss their applicability and usefulness in different problems. To make our discussion simpler, we assume here that the considered metasurface is purely electric, with no magnetic conductivity tensor and no magneto-electric coupling.

In the literature, different methods have been used to model a metasurface as a surface impedance sheet depending on the specific problem at hand. These are generally based on either "one-sided" or "two-sided" surface-impedance conditions. In the one-sided surface-impedance modeling approach (Figure 3A), the metasurface, and the entire half-space behind it, which may include multiple layers, is modeled as a single impenetrable impedance sheet that acts as the load of a transmission line representing propagating/evanescent waves impinging on the metasurface (Figure 3A, right). Clearly, this model is suitable to study metasurfaces operating in reflection mode and, more generally, to problems that are concerned with the back-scattering properties of a multilayered system, as in the classical problem of calculating the modified emission rate (Purcell factor or PF) of a point dipole above a stratified medium [51]. In the one-sided surface-impedance approach, the boundary conditions in Eq. (1) can be reduced to $\hat{\mathbf{z}}\times\mathrm{H}^1=\underline{\boldsymbol{\sigma}}_e\cdot\mathrm{E}_\mathrm{T}^1$, where a surface impedance tensor $\underline{\mathrm{Z}}_s$ can be introduced as $\underline{\mathrm{Z}}_s=\underline{\boldsymbol{\sigma}}_e^{-1}$, which is generally "spatially dispersive" (namely, it depends on the incident wavevector) [46]. As an example, for a metasurface composed of square periodic elements, the conductivity tensor is given by [54]

$$\underline{\boldsymbol{\sigma}}_e=K[(Z_s^{TE}k_x^2+Z_s^{TM}k_y^2)\hat{x}\hat{x}+(Z_s^{TM}k_x^2+Z_s^{TE}k_y^2)\hat{y}\hat{y}+(Z_s^{TE}-Z_s^{TM})k_xk_y(\hat{x}\hat{y}+\hat{y}\hat{x})] \quad (4)$$

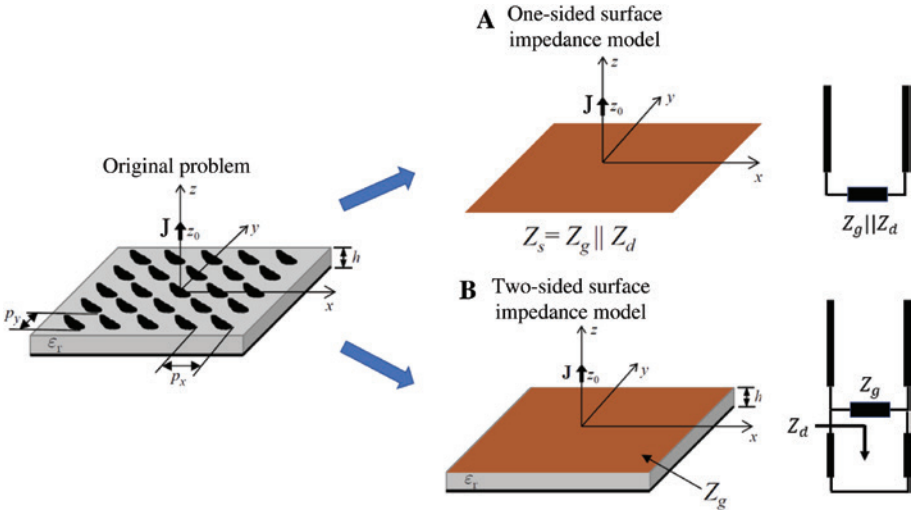

Figure 3: Modeling of metasurfaces in terms of surface-impedance sheets.
Left: Original problem of a metasurface (planar array of meta-atoms) in a host structure (in this example, a grounded slab). Right: Two models in terms of surface-impedance sheets based on different forms of boundary conditions, as discussed in the text: (A) one-sided surface-impedance model and (B) two-sided surface-impedance model, with the corresponding transmission-line representation shown on the right (thick lines represent transmission-line segments and black boxes indicate lumped impedances). A generic point sources is depicted above the metasurface. Adapted with permission from Ref. [46].

where $K = 1/(Z_s^{TE} Z_s^{TM} k_T^2)$, and Z_s^{TE} and Z_s^{TM} indicate the parallel connection of the metasurface impedance Z_g and the input impedance of the entire region below the surface Z_d (namely, $Z_s = Z_g \| Z_d$, where $\|$ indicates a parallel connection, as indicated in Figure 3A). In general, these impedances are different for TE and TM incidence. The expressions for the metasurface impedances, Z_g^{TE} and Z_g^{TM}, for typical metallization patterns can be found in Refs. [41, 42], and the transmission and reflection coefficients entering the Green's function expansion in Eq. (3), as a function of surface impedance, are given in Ref. [46]. Moreover, as mentioned above, the one-sided surface-impedance tensor is generally spatially dispersive, which should be taken into account when calculating the power flow along the surface, as thoroughly discussed in Ref. [55] for a one-sided surface impedance model of a patterned metallic cladding over a grounded dielectric substrate.

The "two-sided surface-impedance method" instead simply models the metasurface as an impedance sheet Z_g, suspended in a host medium or host structure, and considers both the wave reflected and transmitted by the metasurface. An example is depicted in Figure 3B for the specific case of a metasurface on a grounded dielectric slab. This is clearly the method of choice for metasurfaces operating in transmission mode, for example, metasurfaces acting as flat lenses, designed to control the shape of the transmitted wavefront. For this modeling approach, the boundary conditions on the metasurface remain as in Eq. (1), with average fields on the right-hand side of the equations, $\mathrm{J}_e^s = \underline{\boldsymbol{\sigma}}_e \cdot \mathrm{E}_\mathrm{T}^{\mathrm{avg}}$ and $\mathrm{J}_m^s = \underline{\boldsymbol{\sigma}}_e \cdot \mathrm{H}_\mathrm{T}^{\mathrm{avg}}$. The metasurface impedance tensor is again introduced as $\underline{\mathrm{Z}}_s = \underline{\boldsymbol{\sigma}}_e^{-1}$. We also would like to note that, if, by applying this modeling approach, the obtained metasurface impedance inherently depends on the surrounding environment (e.g. the substrate), it is a clear sign that the employed metasurface homogenization process is inadequate (metamaterial or metasurface constitutive parameters are properly defined and meaningful only if they are an inherent property of the homogenized structure, independent of the surrounding environment [29, 56]).

In summary, when applied to the same geometry, as in Figure 3, either modeling approach, one-sided or two-sided, leads to identical results in terms of reflected fields. Therefore, to calculate the fields in the region that contains the source (backscattering or reflection problems), one can choose either the one-sided or the two-sided surface-impedance method. Instead, when calculating the transmitted fields through the metasurface, one needs to use the two-sided surface impedance approach and explicitly consider the presence of other layers behind the metasurface. In other words, the difference between these two modeling approaches originates from the two different forms of boundary conditions one may consider. In the case of one-sided surface impedance, there is no transmitted field, so the surface impedance we need to consider just connects the electric and magnetic fields above the impedance sheet, which therefore acts as the load of a transmission-line model of the structure under

consideration (Figure 3A, right). In this case, the impedance of this load is composed of the actual metasurface impedance in parallel with the input impedance of the region below the metasurface. Conversely, in the two-sided surface-impedance method, the boundary conditions connect the electric and magnetic fields at the two sides of the metasurface through just the impedance of the metasurface itself, which therefore acts as a shunt impedance in a transmission-line model of the structure (Figure 3B, right). We refer the reader to Ref. [46] for additional details on these modeling approaches.

The idea of modeling a metasurface as a surface impedance suspended in free space has been used in Ref. [16] to derive "efficiency limits" on the ability of a generic passive metasurface to control the amplitude and phase of a propagating wave transmitted through it. In particular, for a single purely-electric metasurface, it was found that, (i) if the metasurface is isotropic, namely, with a scalar surface impedance, then the phase of the transmission coefficient t can be controlled only in a limited range [–90°, 90°] by varying the local properties of the metasurface, whereas, (ii) if the metasurface is anisotropic, with a tensorial impedance and polarization coupling, then the cross-polarized transmission phase $\angle t_{xy}$ can be arbitrarily controlled, but its amplitude $|t_{xy}|$ cannot exceed 0.25 for any transmission phase [16]. This fact sets a strict limit on the ability of inhomogeneous purely-electric metasurfaces to mold a propagating wavefront, namely, their ability to act as flat lenses. The efforts to go beyond these limits have led to more advanced metasurface designs operating in transmission mode: (i) multiple electric metasurface layers, inspired by radiofrequency transmit-arrays [16, 19], (ii) metasurfaces with magnetic, in addition to electric, response, realizing so-called "Huygens metasurfaces" that enable zero reflection (due to impedance matching to the surrounding medium) and ideal control of the transmission phase [18, 20–22], and (iii) metasurfaces with tailored bianisotropy and spatial dispersion for more general field transformations [24–26]. These ideas are currently at the basis of modern metasurfaces acting as flat optical/microwave components for far-field illumination.

3 Controlling source radiation and surface-wave propagation on engineered metasurfaces

In the previous section, we have reviewed the analytical techniques that are used to study homogenized metasurfaces under far-field or near-field illumination. An analysis of this type is valid for both isotopic and anisotropic metasurfaces provided that the homogenization conditions defined above are met. Using these methods, one can analyze the reflection/transmission response of arbitrary metasurfaces as well as the excitation of guided waves and leaky waves propagating along the artificial surface.

As mentioned in Section 1, metasurfaces have enabled unprecedented flexibility in controlling and molding the phase, amplitude, and polarization of propagating waves. Another possibility enabled by engineered metasurfaces that is gaining significant attention is represented by their ability to (a) enhance and control the radiation/emission of localized sources in the near field and (b) guide part of the radiated energy in arbitrary directions along the surface, through the controlled coupling with engineered surface modes, as illustrated in Figure 1. In this section, we review these exciting possibilities and their implementations based on 2D structures and materials.

3.1 Metasurfaces and ultrathin planar structures to control the emission rate of a localized emitter

One of the cornerstones of the field of nanophotonics is represented by the ability of controlling and tailoring the photonic emission of an excited atom/molecule or quantum dot (theoretically, a point source), by engineering the surrounding environment, a phenomenon known as the Purcell effect [51]. When placed in the vicinity of an optical/electromagnetic emitter, a metasurface, together with the surrounding medium, forms the environment that interacts with the source. Depending on the metasurface properties, the emission rate of the source can be modified owing to the inhibited or enhanced density of available states for photons, i.e. the photonic local density of states (LDOS), given by $\rho_{\mathrm{LDOS}} = (6/\pi\omega)\mathrm{Im}[\hat{\mathbf{n}}\cdot\underline{\mathbf{G}}(r, r, \omega)\cdot\hat{\mathbf{n}}]$, where $\hat{\mathbf{n}}$ represents the point-source polarization unit vector, and $\underline{\mathbf{G}}(r, r, \omega)$ is the total dyadic Green's function at the source location [namely, the free-space Green's function plus the scattered/reflected Green's function given in Eq. (3)]. Based on the Green's function analysis presented above, it is then relatively straightforward to investigate the effect of metasurfaces and any other stratified planar systems on the local density of photonic states, the spontaneous emission rate (i.e. the decay rate of a quantum emitter upon emission of photons due to interaction with the fluctuating electromagnetic vacuum field), and the so-called Purcell factor $\mathrm{PF} = (6\pi/k_0^3)\mathrm{Im}[\hat{\mathbf{n}}\cdot\underline{\mathbf{G}}(r, r, \omega)\cdot\hat{\mathbf{n}}]$ (i.e. the spontaneous emission rate with respect to the free-space scenario) [51].

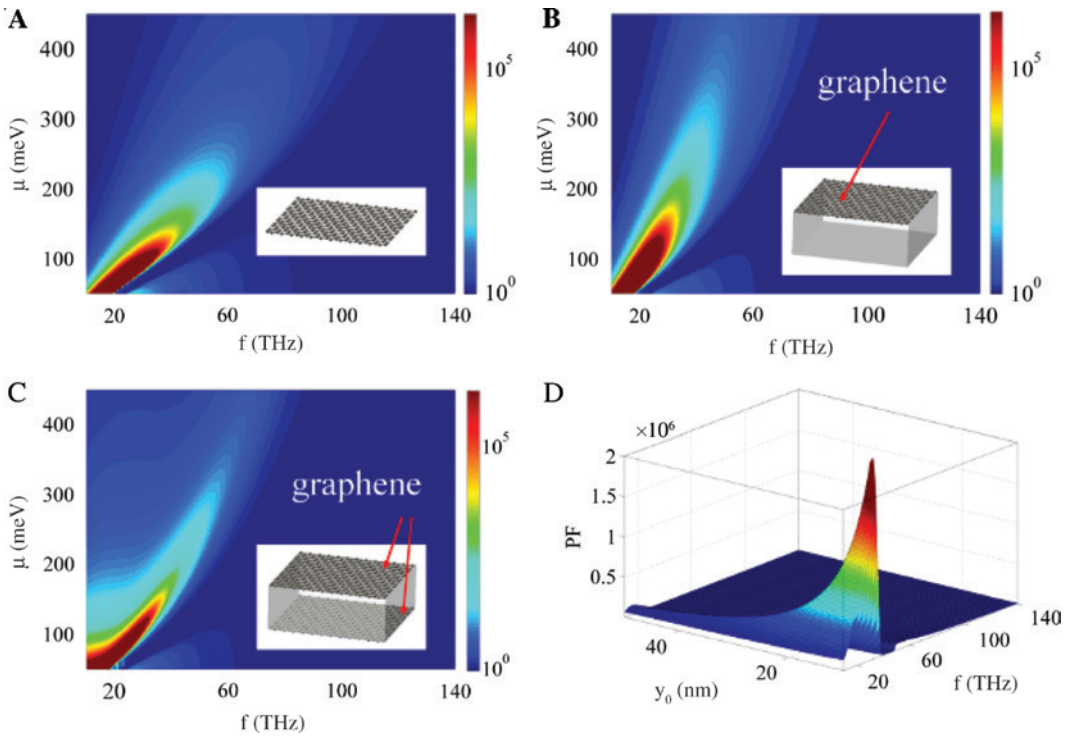

Figure 4: Emission-rate manipulation using graphene-based ultrathin planar structures.
(A) PF for a suspended graphene layer in vacuum with a point source at 10 nm above the surface. (B) PF for graphene on a substrate with thickness $d_s = 10$ nm, $\epsilon = 4$ and (C) for two layers of graphene separated by a 10 nm, $\epsilon = 4$ spacer. (D) PF as a function of position (y_0 is the point-source position above the surface) and frequency for the case in (b). Adapted with permission from Ref. [60].

Indeed, metasurfaces have recently attracted interest in the context of spontaneous emission control due to their guiding properties, optical resonances, and high field enhancements [57–60]. Recent works have investigated the LDOS enhancement due to metasurfaces composed of lattices of discrete magnetoelectric scatterers [59] and the possibility of controlling the LDOS of a source on different graphene-based planar structures [60]. As an example, Figure 4A shows the tunability of the PF for a suspended graphene monolayer over a range of chemical potentials. It is clear that, in the low terahertz regime, the LDOS and PF can be tuned considerably by an external voltage bias. Figure 4B and C shows the PF for a graphene layer supported by a thin substrate and for a metasurface composed of two layers of graphene (a parallel plate-like waveguide). Finally, Figure 4D shows the PF as a function of source position and frequency.

3.2 Hyperbolic metasurfaces: extreme anisotropy on a surface

Simple isotropic metasurfaces (i.e. metasurfaces with scalar, not tensorial, conductivity) can support surface modes that are launched isotropically on the surface by a point source in the near field, resulting in in-plane omnidirectional surface-wave propagation (or quasi-omnidirectional depending on the orientation of the point dipolar source). In general, isotropic or weakly anisotropic metasurfaces do not allow realizing the idea illustrated in Figure 1 of launching and controlling electromagnetic energy from the source location toward specific targets. In drastic contrast to the isotropic case, strongly anisotropic metasurfaces enable the ability of guiding the radiated energy along determined propagation channels on the metasurface [61–65], as we will see in the following. In this context, hyperbolic metamaterials and metasurfaces are uniaxial structures with extreme anisotropy characterized by an effective material tensor (metamaterial) or conductivity/impedance tensor (metasurface) with components having opposite sign for orthogonal electric field polarizations [63, 64] (the term “uniaxial” refers to anisotropic systems characterized by a diagonal constitutive tensor in a suitable coordinate system, with one diagonal element different from the others). As further discussed in the following, hyperbolic metamaterials/metasurfaces exhibit hyperbolic dispersion for wave propagation, as opposed to the usual elliptic dispersion, essentially combining the

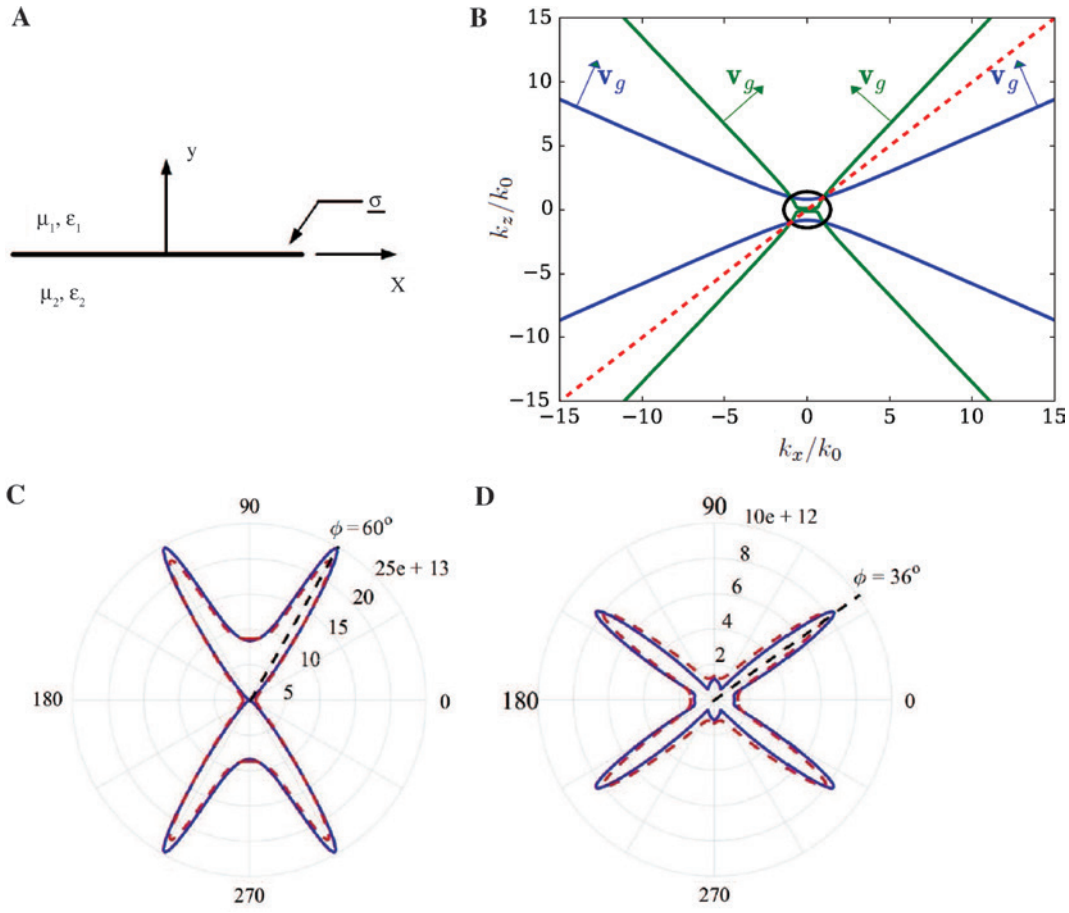

Figure 5: Anisotropic and hyperbolic metasurfaces.
(A) Anisotropic surface with conductivity tensor $\underline{\boldsymbol{\sigma}}$ at the interface of two isotropic materials. (B) Equifrequency contours, $\omega(k) = \text{const}$, for hyperbolic metasurfaces having $\sigma_{xx} = 0.003 + 0.25i$ mS and $\sigma_{zz} = 0.03–0.76i$ mS (blue hyperbola) and $\sigma_{xx} = 1.3 + 16.9i$ mS and $\sigma_{zz} = 0.4–9.2i$ mS (green hyperbola). For comparison, the isotropic case for $\sigma_{xx} = \sigma_{zz} = 0.03–0.76i$ mS (black circle) is also shown. The red dashed line at 45° with respect to the *x*-axis is plotted for visual guidance. (C) Polar plot of the electric field amplitude $|E_y|$ excited by a *y*-directed dipole current above a graphene strip array, assuming chemical potential $\mu_c = 0.45$ eV, width strip $W = 56.1$ nm, periodicity $L = 62.4$ nm, which yields $\sigma_{xx} = 0.003 + 0.25i$ mS and $\sigma_{zz} = 0.03–0.76i$ mS [blue hyperbola in (B)]. (D) Similar to (C), but for a graphene-strip array with $\mu_c = 1$ eV, $W = 196$ nm and $L = 200$ nm, and $\sigma_{xx} = 1.3 + 16.9i$ mS and $\sigma_{zz} = 0.4–9.2i$ mS [green hyperbola in (B)]. Plots in (C) and (D) are calculated at frequency $f = 10$ THz, $\rho = 0.2\lambda$ (radial distance from source) and $y = 0.005\lambda$ (vertical distance from the surface). Solid blue line is for numerical calculation of the Green's function, and dashed red line for residue-branch-cut evaluation. Adapted with permission from Ref. [64].

response of transparent dielectrics and reflective metals in different directions [66]. In the context of 3D metamaterials, these exotic properties have led to new physical effects and novel optical devices for a wide range of applications, such as subwavelength imaging, nanolithography, light-emission engineering [66], negative-index waveguides [67], subdiffraction photonic funnels [68], and novel nanoscale resonators [69]. While the complexity of fabrication of 3D metamaterials, and their sensitivity to losses, have hindered the impact of these concepts, especially in the terahertz and optical regime [63, 64], planar metasurfaces may overcome many of these challenges [9, 15], offering a practical route to realize extreme hyperbolic dispersion.

Figure 5A shows a schematic of the geometry under consideration, which contains a hyperbolic metasurface with the following conductivity tensor:

$$\underline{\boldsymbol{\sigma}} = \begin{pmatrix} \sigma_{xx} & 0 \\ 0 & \sigma_{zz} \end{pmatrix} \tag{5}$$

at the interface of two different media with electric permittivity and magnetic permeability ϵ_1, μ_1 and ϵ_2, μ_2. Although here the conductivity tensor is assumed to be diagonal, hence representing a uniaxial metasurface, in a general scenario, off-diagonal conductivity tensor elements may arise if the subwavelength meta-atoms are nonsymmetrical with respect to the coordinate system [21, 28, 65], or

because of the presence of magneto-optical effects [51, 65], or also nonlocal effects due to finite Fermi velocity of the electrons in the metasurface elements [65, 70]. In the interest of clarity, here we only focus on diagonal conductivity tensors. For a point source radiating above the metasurface, the complete electromagnetic response could be computed using the general formalism provided in the previous section. Although the numerical evaluation of the Green's function (3) can be challenging [46, 62], advanced techniques based on complex analysis to efficiently perform the integration have been reported in the literature (see, e.g. Ref. [64]). In particular, it was shown in Ref. [64] that the 2D integral in Eq. (3) can be reduced to (i) a pole residue associated with the surface-wave contribution (representing the surface mode propagating on the metasurface) and (ii) a branch-cut integral associated with the so-called continuous-spectrum contribution (representing the radiation into the surrounding environment) [71, 72]. These two contributions represent well the electromagnetic response of the system: part of the energy radiated by the point dipole is coupled into the guided surface modes of the metasurface, whereas the rest is directly radiated into the environment.

To better understand the behavior of surface modes supported by an anisotropic hyperbolic metasurface with conductivity (5), it is insightful to inspect the surface-wave dispersion relation [64]:

$$D(k_x, k_z) = 2\sigma_{xx}(k^2 - k_x^2) + 2\sigma_{zz}(k^2 - k_z^2) - j4\frac{k}{\eta}p\left(1 + \frac{1}{4}\eta^2\sigma_{xx}\sigma_{zz}\right) \quad (6)$$

where $\epsilon_1 = \epsilon_2 = \epsilon$, $\mu_1 = \mu_2 = \mu$, $k = \omega(\epsilon\mu)^{1/2}$, $\eta = (\mu/\epsilon)^{1/2}$, and $a = (k_x^2 + k_z^2 - k^2)^{1/2}$ is the vertical attenuation of the surface wave. One of the main differences between surface modes in isotropic and anisotropic metasurfaces is that, in the isotropic case, surface modes could be found in the form of pure TE or pure TM modes, whereas the modes of anisotropic metasurfaces are always a mixture of TE and TM field contributions. In addition, in an anisotropic structure, the direction of energy flow, defined by the group velocity vector [73], is not necessarily parallel to the direction of the wavevector k. As usually done, the direction of energy flow (equal to the group velocity in low-loss regions) can be determined by examining the "equifrequency surface" (EFS), $\omega(\mathrm{k}) = \mathrm{const}$, of the surface mode [64]. Because the group velocity is defined as the gradient of the dispersion function $\omega(\mathrm{k})$ with respect to wavevector (i.e. $\nabla_{\mathrm{k}}\omega(\mathrm{k})$), the direction of energy flow is necessarily orthogonal to the EFS contours. Assuming that the conductivity is purely imaginary and lossless, $\sigma_{ii} = j\sigma''_{ii}$, $i = x$, z, and that k_x, $k_z \gg k$, the zeros of Eq. (6) can be approximated as the solution of [64]

$$\frac{k_x^2}{\sigma''_{zz}} + \frac{k_z^2}{\sigma''_{xx}} = 2a\omega\left(\frac{\varepsilon}{\sigma''_{xx}\sigma''_{zz}} - \frac{\mu}{4}\right). \quad (7)$$

At a given frequency ω, this equation may describe either an ellipse or a hyperbola in the $k_x - k_y$ plane depending on the relative sign of the two conductivity components. For example, "elliptic EFS topology" arises when $\sigma''_{xx} \cdot \sigma''_{zz} > 0$ corresponding to the black curve in Figure 5B. The length of the ellipse's principal axes along k_x and k_z is proportional to σ''_{zz} and σ''_{xx}, respectively. In this case, the modes might be associated with quasi-TM (inductive surface $\mathrm{Im}[\sigma_{xx}] > 0$, $\mathrm{Im}[\sigma_{xx}] > 0$) or quasi-TE (capacitive surface $\mathrm{Im}[\sigma_{xx}] < 0$, $\mathrm{Im}[\sigma_{xx}] < 0$) polarization [65] [as mentioned above, the character of the modes can be purely TE or TM only if the metasurface is isotropic ($\sigma_{xx} = \sigma_{zz}$)]. It was shown in Ref. [65] that the quasi-TE surface modes present a free-space like dispersion, leading to weak light-matter interaction, whereas the quasi-TM modes exhibit more confinement near the surface and, therefore, stronger interaction.

If one of the two conductivity tensor components changes sign, such that $\sigma''_{xx} \cdot \sigma''_{zz} < 0$, then the topology of the equifrequency contour drastically changes and becomes "hyperbolic". In this regime, the anisotropic metasurface behaves like a dielectric in one direction and a metal in the orthogonal direction. Two examples of hyperbolic EFS are shown in Figure 5B for two values of surface conductivity (blue lines: $\sigma_{xx} = 0.003 + 0.25i$ mS and $\sigma_{zz} = 0.03 - 0.76i$ mS and green lines: $\sigma_{xx} = 1.3 - 16.9i$ mS and $\sigma_{zz} = 0.4 - 9.2i$ mS). The hyperbola asymptotes are defined by $k_z = \pm k_x\sqrt{|\sigma''_{xx}/\sigma''_{zz}|}$, and the direction of energy flow of the surface mode is given by the angle [63, 64]

$$\phi = \tan^{-1}\sqrt{-\frac{\sigma''_{zz}}{\sigma''_{xx}}} \quad (8)$$

which is defined with respect to the z-axis (note that this is valid only in the hyperbolic regime in the asymptotic region, namely, for large enough wavenumber). A simple interpretation of the above equation is that the energy tends to flow mostly toward the direction with lower imaginary conductivity component [63].

Considering that the field radiated by a point dipole has, in theory, an infinite angular spectrum, containing all possible values of transverse wavenumber, this near-field illumination can excite a continuous set of surface modes, with different wavenumber, according to the EQS in Figure 5B (we also would like to note that this hyperbolic

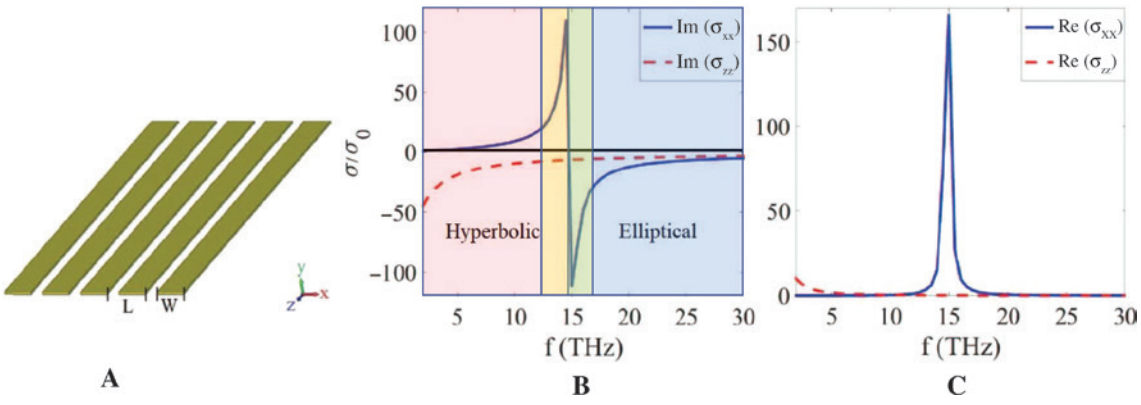

Figure 6: Graphene-based anisotropic and hyperbolic metasurfaces.
(A) Array of graphene strips of width W and period L. (B) Imaginary parts of σ_{xx} and σ_{zz} and (C) real parts of σ_{xx} and σ_{zz} (normalized by $\sigma_0 = e^2/4\hbar$) for a graphene-strip array with $\tau = 0.35$ ps, $\mu_c = 0.33$ eV, $W = 59$ nm and $L = 64$ nm. Region 1 (light red) is hyperbolic and region 2 (light blue) is anisotropic with elliptical dispersion. The yellow/green transition region is characterized by high losses in the x-direction. Adapted with permission from Ref. [64].

EQS has no cutoff at high values of spatial frequency, due to the "open" shape of the hyperbola, in drastic contrast with conventional elliptic dispersion; in practice, however, any realistic hyperbolic metasurface exhibits a high spatial-frequency cutoff, where the hyperbolic curve "closes" due to the effect of nonlocality, as the high spatial frequencies start "seeing" the discrete nature of the metasurface [70]). Because the vectors normal to the hyperbola point in roughly the same direction for a given sign of k_x and k_z, a dipole source will excite a narrow surface-wave beam confined on the surface of a hyperbolic metasurface [64]. For example, the asymptotes of the blue hyperbola in Figure 5B have an angle of 30° with respect to the z-axis, and thus the normal to the hyperbola (i.e. the group velocity vector) is pointing at 60° with respect to the z-axis.

As an example, an hyperbolic metasurface with the conductivity tensor corresponding to the blue hyperbola in Figure 5B can be implemented with an array of graphene strips, as shown in Figure 6A, with chemical potential $\mu_c = 0.45$ eV, strip width $W = 56.1$ nm, and periodicity $L = 62.4$ nm [64]. For this physical implementation, the electric field profile of the surface modes has been obtained in Ref. [64] using two methods: (i) numerically solving the Green's function in Eq. (3), which is a computationally demanding operation, and (ii) using a faster residue-branch-cut evaluation, as discussed at the beginning of this section. The results are reported in Figure 5C, showing that the two methods are in good agreement, hence justifying the faster evaluation in terms of residue and branch-cut contributions. As can be seen, most of the surface-wave energy is flowing toward $\phi = 60°$ from the z-axis (and mirror-symmetric directions with respect to the two axes), confirming the response predicted by the hyperbolic equifrequency contours. Figure 5D also shows a different case with energy flow toward an angle $\phi = 36°$, corresponding to the steeper green hyperbola in Figure 5B. This response can be realized with an array of graphene strips having $\mu_c = 1$ eV, $W = 196$ nm, and $L = 200$ nm [64].

Another case of particular relevance is when the hyperbolic metasurface exhibits an extreme anisotropy in which the imaginary conductivity along a specific direction becomes very small compared to the one in the orthogonal direction, $|\sigma''_{zz}| \ll |\sigma''_{xx}|$, which is sometimes called the "canalization regime". In this extremely anisotropic hyperbolic metasurface, the hyperbolic equifrequency contour tends to become flat, which implies that any surface wave excited by a near-field source, with any transverse wavenumber k_x, would mostly propagate along the z-axis, yielding a narrow "diffraction-less" surface-wave beam that almost does not spread out as it propagates along the surface [74]. In practice, this scenario may again be implemented with a suitably engineered array of parallel graphene nanoribbons having complex conductivities. An analogous implementation has been studied in Ref. [74]: as shown in Figure 7A, the negative and positive conductivities are created electronically by gating a graphene layer over a triangularly corrugated plane. Figure 7C and D shows the electric field amplitude distribution for two point sources, separated by a subwavelength distance, on the plane $z = 0$ over the modulated-graphene metasurface and over a homogenous graphene layer, respectively, clearly showing the surface-wave canalization in the modulated case. This behavior is of clear interest for imaging applications, as the surface waves avoid the usual diffraction expected on a homogeneous layer, allowing to

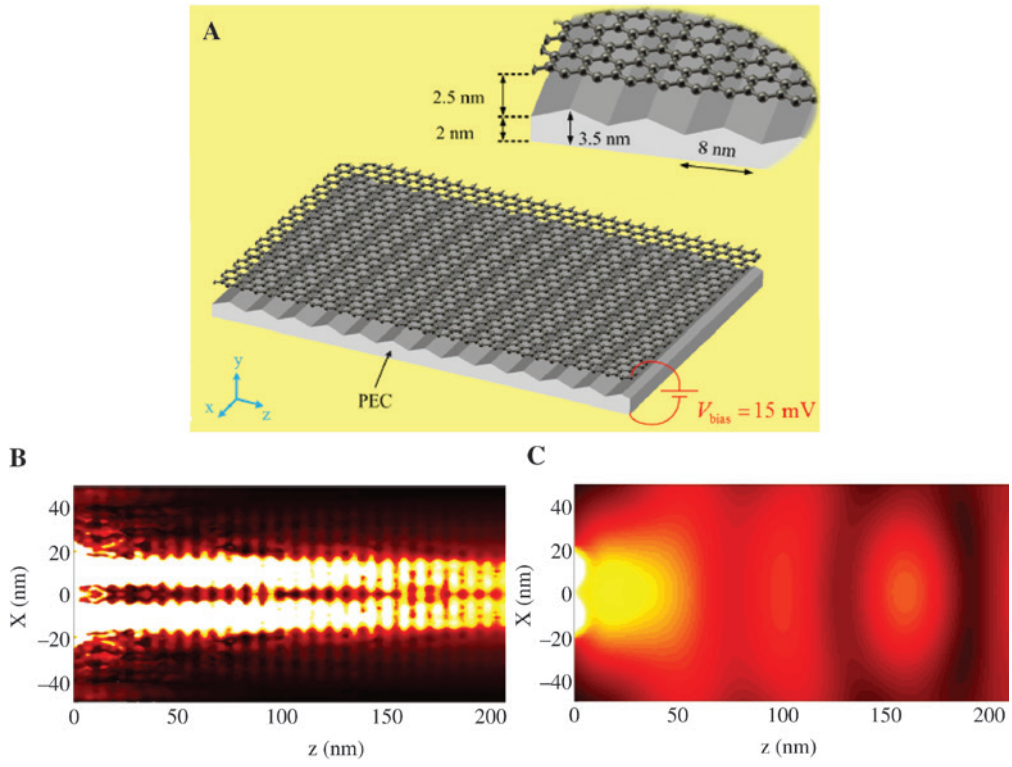

Figure 7: Surface-wave canalization on a modulated-graphene metasurface.
(A) A graphene monolayer with fixed gating voltage over a triangularly perturbed ground plane that realizes a tailored conductivity modulation. (B and C) Amplitude of the vertical component of the electric field for the surface plasmon polaritons launched by two closely located point sources over (B) modulated graphene and (C) homogeneous graphene. Adapted with permission from Ref. [74].

distinguish the two point sources even at a large distance from the source plane.

Further details on the use of graphene, and other 2D materials, to implement metasurfaces with extreme anisotropy are discussed in the next section.

3.3 2D Materials as anisotropic and hyperbolic metasurfaces

The most straightforward approach to realize uniaxial and hyperbolic metasurfaces is to reduce the profile of well-known bulk uniaxial materials resulting in thin layers that essentially act like 2D metasurfaces [65]. Even more interesting, the emerging class of 2D atomic crystals [75] represents the ultimate embodiment of metasurfaces in terms of thinness, combined with exciting performance in terms of tunability, flexibility, quality factor, etc. [64]. Some notable examples of 2D layered crystals include graphene and transition metal dichalcogenides and trichalcogenides [64]. Another crystal with similar properties is magnesium diboride, in which graphene-like layers of boron are alternated by densely packed layers of magnesium [65, 76]. Hexagonal boron nitride (hBN) should also be mentioned as another promising material in this category [65], especially due to its excellent compatibility with graphene optoelectronics [77]. Notably, hBN has allowed the experimental demonstration of low-loss hyperbolic phonon polaritons in the infrared [78, 79].

One of the most popular approaches to realize uniaxial and hyperbolic metasurfaces at terahertz and infrared frequencies is the use of dense arrays of graphene strips [63, 80], as shown in Figure 6A. The dispersion topology of this structure may range from elliptical to hyperbolic as a function of its geometrical and electrical parameters. The in-plane effective conductivity tensor of this graphene-based metasurface can be analytically calculated using an effective medium theory, obtaining [63]

$$\sigma_{zz}^{\text{eff}} = \sigma \frac{W}{L} \text{ and } \sigma_{xx}^{\text{eff}} = \frac{L\sigma\sigma_c}{W\sigma_c + G\sigma} \tag{9}$$

where L and W are the period and width of the strips, respectively, $G = L - W$ is the separation distance between two consecutive strips, σ is the conductivity of homogeneous graphene, and $\sigma_c = j\frac{\omega\varepsilon_0 L}{\pi}\ln\left(\csc\frac{\pi G}{2L}\right)$ is an equivalent

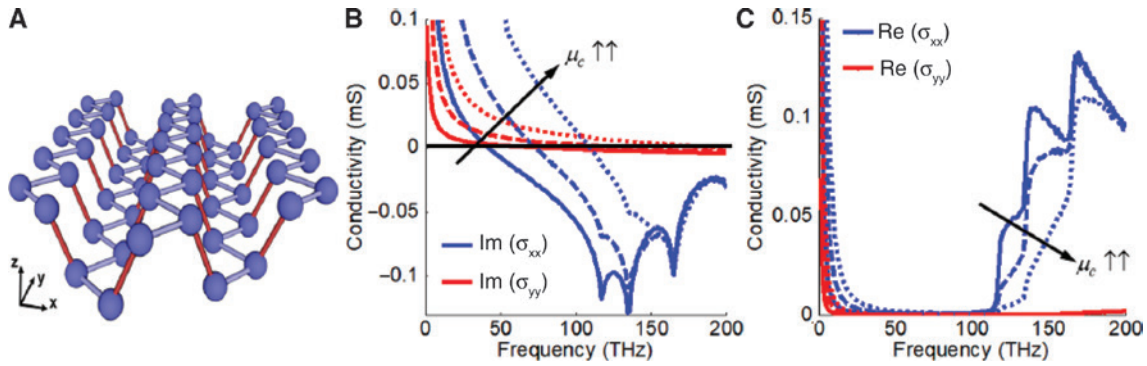

Figure 8: Naturally anisotropic 2D materials: the case of black phosphorus (BP).
(A) Lattice structure of monolayer BP. Different colors are used for visual clarity. (B) Imaginary part of BP conductivity components versus frequency for several values of chemical potential. (C) Real part of BP conductivity components versus frequency for several values of chemical potential. Solid, dashed, and dotted lines correspond to chemical potentials of 0.005, 0.05, and 0.1 eV, respectively. The considered BP thickness is 10 nm, its direct band gap is 0.485 eV, damping 5 meV, at a temperature of 300 K. Adapted with permission from Ref. [65].

conductivity associated with the near-field coupling between adjacent strips, obtained using an electrostatic approach [81]. These effective parameters are valid only when the homogenization condition $L \ll \lambda_{SW}$ is satisfied, where λ_{SW} is the wavelength of the guided surface wave in the in-plane direction perpendicular to the strips (x in this case), thus leading to a homogeneous 2D metasurface [64]. Figure 6B and C shows the real and imaginary parts of σ_{xx} and σ_{zz} in a wide range of frequencies in the terahertz range, for a graphene-strip array with scattering time $\tau = 0.35$ ps, chemical potential $\mu_c = 0.33$ eV, and geometrical parameters $W = 59$ nm and $L = 64$ nm. As can be seen in Figure 6, the effective conductivities are mostly imaginary, except in the resonant lossy window near 15 THz. Most importantly, at frequencies below the resonance, the imaginary conductivities have opposite signs in the two directions, whereas they are both negative above the resonance. As a result, this structure can exhibit both a hyperbolic response at low frequencies and a nonhyperbolic (but still anisotropic) response at higher frequencies, separated by a lossy region in which surface waves are strongly attenuated.

Another promising material platform for metasurfaces is represented by BP, which is also a layered material, similar to graphite, with each layer forming a "wrinkled" surface [64], as depicted in Figure 8A. BP is a thermodynamically stable phase of phosphorus at ambient temperature and pressure [82], and it has recently been exfoliated into its multilayers [83, 84]. BP possesses exciting optical and electrical properties, such as an intrinsic direct band gap that may range from ~2 eV in monolayers (phosphorene) to 0.3 eV in its bulk configuration; tunable electric response versus thickness, or via externally applied electric/magnetic fields and mechanical strain; and the possibility to support confined surface plasmons in the mid-infrared to near-infrared range [64, 65]. Similar to the case of graphene, the ultrathin nature of BP allows a simple electromagnetic characterization in terms of optical conductivity, which may be accurately derived applying the well-known Kubo formalism [85, 86]. Figure 8B and C shows the real and imaginary parts of the BP conductivity components.

Remarkably, a thin film of BP is an example of a natural hyperbolic metasurface. In fact, Figure 8B and C shows that, in the low-loss region where the conductivity is almost purely imaginary, BP can behave as either a hyperbolic or an elliptical anisotropic surface depending on the frequency and chemical potential. However, although BP exhibits a hyperbolic regime, the resulting values of conductivity are rather small; therefore, although a hyperbolic surface plasmon can be excited, this is generally not the dominant response, as discussed in Ref. [64]. Larger values of conductivities can be obtained in the nonhyperbolic (Drude) regime. For example, a 10-nm-thick BP film with electron doping level $10 \times 10^{13}/\text{cm}^2$ has conductivity tensor components $\sigma_{xx} = 0.0008 - 0.2923i$ and $\sigma_{zz} = 0.0002 - 0.0658i$ mS at $f = 92.6$ THz. As shown in Figure 9, this highly anisotropic, but nonhyperbolic, surface can support a directional surface wave mainly directed along one of the coordinate axes and tightly confined on the surface. In particular, Figure 9A shows the electric field profile of the surface plasmon polariton excited by a point source above the surface, calculated by numerically solving Maxwell's equations using a finite-difference time-domain method (FDTD) provided by a commercial software (Lumerical [87]). Figure 9B shows the vertical variation of the field distribution calculated by Lumerical, showing strong light confinement near the surface.

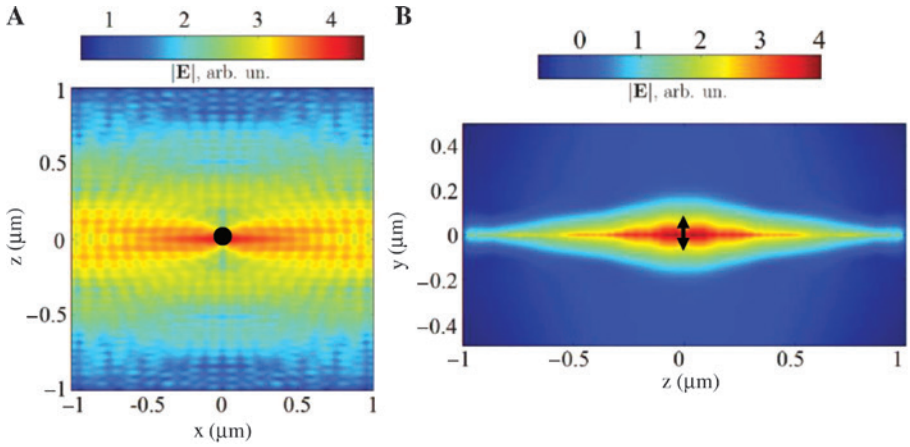

Figure 9: Directional surface plasmon polaritons on anisotropic black phosphorus (BP).
Field intensity distribution excited by a *y*-directed dipole current source on a 10-nm-thick BP layer with doping level $10\times10^{13}/\text{cm}^2$ at $f=92.6$ THz. (A) In-plane field distribution and (B) vertical out-of-plane field distribution, dominated by the response of a surface plasmon polariton mainly directed along the *x*-axis and tightly confined on the surface. Both figures are calculated with a commercial FDTD solver. The black dot/arrow indicates a *y*-polarized dipole. Adapted with permission from Ref. [64].

4 Conclusion

In this review article, we have discussed some exciting research directions in the emerging field of metasurfaces, with particular focus on the theoretical aspects of artificial engineered surfaces and their interaction with near-field sources. We have reviewed the analytical modeling of metasurfaces in terms of homogenized effective surface conductivities/impedances, and presented the stricter homogenization conditions for the case of near-field excitation, and some performance limits of electric metasurfaces. We have then discussed the possibility of controlling the emission/radiation from localized sources near an artificial surface, as well as the exciting possibility of guiding a portion of the radiated energy along the interface through a controlled coupling with the surface modes of the metasurface. In this context, particular attention has been devoted to surfaces with extreme anisotropy, known as hyperbolic metasurfaces, which enable unusual beam-like surface-wave propagation, and the possibility of imaging below the diffraction limit in the so-called canalization regime. Finally, we have discussed the potential of 2D materials, such as graphene and BP, to implement anisotropic and hyperbolic dispersion on ultrathin surfaces.

We believe that the topics reviewed in this article represent some of the most promising and exciting directions in the field of metasurfaces. In the vision outlined here, future generations of metasurfaces will not only act as flat lenses to manipulate propagating waves but also as planar ultrathin platforms to control near-field interactions with localized sources and tailor the propagation of highly confined surface waves in arbitrary directions.

References

[1] Engheta N, Ziolkowski RW. Electromagnetic metamaterials: physics and engineering explorations. New York, NY, USA: Wiley-IEEE Press, 2006.
[2] Monticone F, Alù A. Metamaterial, plasmonic and nanophotonic devices. Rep Prog Phys 2017;80:36401.
[3] Pozar DM. Flat lens antenna concept using aperture coupled microstrip patches. Electron Lett 1996;32:2109.
[4] Munk BA. Frequency selective surfaces: theory and design. New York, John Wiley and Sons, 2000.
[5] Wang SS, Magnusson R, Bagby JS, Moharam MG. Guided-mode resonances in planar dielectric-layer diffraction gratings. J Opt Soc Am A 1990;7:1470.
[6] Bomzon Z, Kleiner V, Hasman E. Pancharatnam-Berry phase in space-variant polarization-state manipulations with subwavelength gratings. Opt Lett 2001;26:1424.
[7] Hasman E, Kleiner V, Biener G, Niv A. Polarization dependent focusing lens by use of quantized Pancharatnam-Berry phase diffractive optics. Appl Phys Lett 2003;82:328.
[8] Holloway CL, Dienstfrey A, Kuester EF, O'Hara JF, Azad AK, Taylor AJ. A discussion on the interpretation and characterization of metafilms/metasurfaces: the two-dimensional equivalent of metamaterials. Metamaterials 2009;3:100–12.
[9] Kuester EF, Mohamed MA, Piket-May M, Holloway CL. Averaged transition conditions for electromagnetic fields at a metafilm. IEEE Trans Antennas Propag 2003;51:2641–51.
[10] Holloway CL, Kuester EF, Novotny D. Waveguides composed of metafilms/metasurfaces: the two-dimensional equivalent of metamaterials. IEEE Antennas Wireless Propag Lett 2009;8:525–9.
[11] Holloway CL, Mohamed MA, Kuester EF, Dienstfrey A. Reflection and transmission properties of a metafilm: with an application to a controllable surface composed of resonant particles. IEEE Trans Electromagn Compat 2005;47:853–65.
[12] Holloway CL, Kuester EF, Dienstfrey A. Characterizing metasurfaces/metafilms: the connection between surface

susceptibilities and effective material properties. IEEE Antennas Wireless Propag Lett 2011;10:1507–11.
[13] Tretyakov S. Analytical modeling in applied electromagnetics. Norwood, MA: Artech House, 2003.
[14] Yu N, Genevet P, Kats M, Aieta F, Tetienne JP, Capasso F, Gaburro Z. Light propagation with phase discontinuities: generalized laws of reflection and refraction. Science 2011;334:333–7.
[15] Yu N, Capasso F. Flat optics with designer metasurfaces. Nat Mater 2014;13:139–50.
[16] Monticone F, Estakhri NM, Alù A. Full control of nanoscale optical transmission with a composite metascreen. Phys Rev Lett 2013;110:203903.
[17] Arbabi A, Arbabi E, Horie Y, Faraon A. Fundamental limits of ultrathin metasurfaces. Sci Rep 2017;7:43722.
[18] Pfeiffer C, Grbic A. Metamaterial Huygens' surfaces: tailoring wave fronts with reflectionless sheets. Phys Rev Lett 2013;110:197401.
[19] Pfeiffer C, Grbic A. Cascaded metasurfaces for complete phase and polarization control. Appl Phys Lett 2013;102:231116.
[20] Selvanayagam M, Eleftheriades GV. Discontinuous electromagnetic fields using orthogonal electric and magnetic currents for wavefront manipulation. Opt Express 2013;21:14409.
[21] Arbabi A, Horie Y, Bagheri M, Faraon A. Dielectric metasurfaces for complete control of phase and polarization with subwavelength spatial resolution and high transmission. Nat Nanotechnol 2015;10:937–43.
[22] Khorasaninejad M, Chen WT, Devlin RC, Oh J, Zhu AY, Capasso F. Metalenses at visible wavelengths: diffraction-limited focusing and subwavelength resolution imaging. Science 2016;352:1190–4.
[23] Asadchy VS, Albooyeh M, Tcvetkova SN, Diaz-Rubio A, Ra'di Y, Tretyakov SA. Perfect control of reflection and refraction using spatially dispersive metasurfaces. Phys Rev B 2016;94:075142.
[24] Pfeiffer C, Grbic A. Emulating nonreciprocity with spatially dispersive metasurfaces excited at oblique incidence. Phys Rev Lett 2016;117:077401.
[25] Epstein A, Eleftheriades G. Arbitrary power-conserving field transformations with passive lossless omega-type bianisotropic metasurfaces. IEEE Trans Antennas Propag 2016;64:3880–95.
[26] Diaz-Rubio A, Asadchy VS, Elsakka A, Tretyakov SA. From the generalized reflection law to the realization of perfect anomalous reflectors. Sci Adv 2017;3:e1602714.
[27] Yu N, Genevet P, Aieta F, et al. Flat optics: controlling wavefronts with optical antenna metasurfaces. IEEE J Sel Top Quant Electron 2013;19:4700423.
[28] Kildishev AV, Boltasseva A, Shalaev VM. Planar photonics with metasurfaces. Science 2013;339:1232009.
[29] Glybovski SB, Tretyakov SA, Belov PA, Kivshar YS, Simovski CR. Metasurfaces: from microwaves to visible. Phys Rep 2016;634:1–72.
[30] Epstein A, Eleftheriades GV. Huygens' metasurfaces via the equivalence principle: design and applications. J Opt Soc Am B 2016;33:A31.
[31] Oliner AA, Jackson DR. Leaky-wave antennas. In: Volakis JL, ed. Antenna Engineering Handbook. New York, NY: McGraw-Hill, 2007.
[32] Monticone F, Alù A. Leaky-wave theory, techniques, and applications: from microwaves to visible frequencies. Proc IEEE 2015;103:793–821.
[33] Minatti G, Martini E, Maci S. Efficiency of metasurface antennas. IEEE Trans Antennas Propag 2017;65:1532–41.
[34] Minatti G, Caminita F, Martini E, Sabbadini M, Maci S. Synthesis of modulated-metasurface antennas with amplitude, phase, and polarization control. IEEE Trans Antennas Propag 2017;64:3907–19.
[35] Maci S, Minatti G, Casaletti M, Bosiljevac M. Metasurfing: addressing waves on impenetrable metasurfaces. IEEE Antennas Wireless Propag Lett. 2011;10:1499–502.
[36] Martini E, Mencagli M, Gonzalez-Ovejero D, Maci S. Flat optics for surface waves. IEEE Trans Antennas Propag 2016;64:155–66.
[37] Martini E, Mencagli MJ, Maci S. Metasurface transformation for surface wave control. Philos Trans R Soc A 2015;373:20140355.
[38] Mencagli M Jr, Martini E, Gonzalez-Ovejero D, Maci S. Metasurface transformation optics. J Opt 2014;16:125106.
[39] Yang R, Hao Y. An accurate control of the surface wave using transformation optics. Opt Express 2012;20:9341–50.
[40] Patel AM, Grbic A. Transformation electromagnetics devices based on printed-circuit tensor impedance surfaces. IEEE Trans Microw Theory Techn 2014;62:1102–11.
[41] Luukkonen O, Simovski C, Granet G, et al. Simple and accurate analytical model of planar grids and high-impedance surfaces comprising metal strips or patches. IEEE Trans Antennas Propag 2008;56:1624–32.
[42] Paulotto S, Baccarelli P, Burghignoli P, Lovat G, Hanson GW, Yakovlev AB. Homogenized Green's functions for an aperiodic line source over planar densely periodic artificial impedance surfaces. IEEE Trans Microw Theory Techn 2010;58:1807–17.
[43] Kaipa CS, Yakovlev AB, Medina F, Mesa F, Butler CA, Hibbins AP. Circuit modeling of the transmissivity of stacked twodimensional metallic meshes. Opt Express 2010;18:13309–20.
[44] Kaipa CS, Yakovlev AB, Medina F, Mesa F. Transmission through stacked 2D periodic distributions of square conducting patches. J Appl Phys 2012;112:033101.
[45] Padooru YR, Yakovlev AB, Chen P-Y, Alù A. Analytical modeling of conformal mantle cloaks for cylindrical objects using subwavelength printed and slotted arrays. J Appl Phys 2012;112:034907.
[46] Liang F, Hanson GW, Yakovlev AB, et al. Dyadic Green's functions for dipole excitation of homogenized metasurfaces. IEEE Trans Antennas Propag 2016;64:167–78.
[47] Holloway CL, Kuester EF, Gordon JA, O'Hara J, Booth J, Smith DR. An overview of the theory and applications of metasurfaces: the two-dimensional equivalents of metamaterials. IEEE Antennas Propag Mag 2012;54:10–35.
[48] Tretyakov SA. Metasurfaces for general transformations of electromagnetic fields. Philos Trans R Soc A 2015;373:20140362.
[49] Hanson GW. Dyadic Green's functions for an anisotropic, nonlocal model of biased graphene. IEEE Trans Antennas Propag 2008;56:747–57.
[50] Holloway C, Love D, Kuester E, Salandrino A, Engheta N. Subwavelength resonators: on the use of metafilms to overcome the $\lambda/2$ size limit. IET Microw Antennas Propag 2008;2:120–9.
[51] Novotny L, Hecht B. Principle of nano-optics. Cambridge, England, Cambridge University Press, 2012.
[52] Monticone F, Alù A. Bound states within the radiation continuum in diffraction gratings and the role of leaky modes. N J Phys 2017;19:093011.

[53] Arvas E, Harrington RF. Computation of the magnetic polarizability of conducting disks and the electric polarizability of apertures. IEEE Trans Antennas Propag 1983;31:719–25.
[54] Holloway CL, Kuester EF. Equivalent boundary conditions for a perfectly conducting periodic surface with a cover layer. Radio Sci 2000;35:661–81.
[55] Patel AM, Grbic A. The effects of spatial dispersion on power flow along a printed-circuit tensor impedance surface. IEEE Trans Antennas Propag 2014;62:1464–9.
[56] Alù A. First-principles homogenization theory for periodic metamaterials. Phys Rev B 2011;84:75153.
[57] Lunnemann P, Koenderink AF. Dispersion of guided modes in two-dimensional split ring lattices. Phys Rev B 2014;90:245416.
[58] Poddubny A, Belov P, Ginzburg P, Zayats A, Kivshar Y. Microscopic model of Purcell enhancement in hyperbolic metamaterials. Phys Rev B 2012;86:035148.
[59] Lunnemann P, Koenderink AF. The local density of optical states of a metasurface. Sci Rep 2016;6:20655.
[60] Forati E, Hanson GW, Hughes A. Graphene as a tunable THz reservoir for shaping the Mollow triplet of an artificial atom via plasmonic effects. Phys Rev B 2014;90:245416.
[61] Ferraria L, Wu C, Lepaged D, Zhang X, Liu Z. Hyperbolic metamaterials and their applications. Prog Quant Electron 2015;40:1–40.
[62] Gomez-Diaz JS, Tymchenko M, Alù A. Hyperbolic metasurfaces: surface plasmons, light-matter interactions, and physical implementation using graphene strips. Opt Mater Express 2015;5:2313–29.
[63] Gomez-Diaz JS, Tymchenko M, Alù A. Hyperbolic plasmons and topological transitions over uniaxial metasurfaces. Phys Rev Lett 2015;114:233901.
[64] Hassani Gangaraj SA, Low T, Nemilentsau A, Hanson GW. Directive surface plasmons on tunable two-dimensional hyperbolic metasurfaces and black phosphorus: Green's function and complex plane analysis. IEEE Trans Antennas Propag 2016;65:1174–86.
[65] Gomez-Diaz JS, Alù A. Flatland optics with hyperbolic metasurfaces. ACS Photon 2016;3:2211–24.
[66] Drachev VP, Podolskiy VA, Kildishev AV. Hyperbolic metamaterials: new physics behind a classical problem. Opt Express 2013;21:15048–64.
[67] Podolskiy VA, Narimanov EE. Strongly anisotropic waveguide as a nonmagnetic left-handed system. Phys Rev B 2005;71:201101(R).
[68] Govyadinov AA, Podolskiy VA. Metamaterial photonic funnels for subdiffraction light compression and propagation. Phys Rev B 2006;73:155108.
[69] Yao J, Yang X, Yin X, Bartal G, Zhang X. Three dimensional nanometer-scale optical cavities of indefinite medium. Proc Natl Acad Sci USA 2011;108:11327–31.
[70] Correas-Serrano D, Gomez-Diaz JS, Tymchenko M, Alù A. Nonlocal response of hyperbolic metasurfaces. Opt Express 2015;23:29434–48.
[71] Chang DC, Kuester EF. An analytic theory for narrow open microstrip. Arch Elek Ubertragungstech 1979;33:199–206.
[72] Nyquist DP, Grimm JM, Infante DJ, Braunisch H. Classification of the proper propagation-mode spectrum and leaky-wave modes on open planar waveguides. Electromagnetics 1997;17:105–30.
[73] Kong J. Electromagnetic wave theory. New York, NY, USA: Wiley-Interscience, 1986.
[74] Forati E, Hanson GW, Yakovlev AB, Alù A. Planar hyperlens based on a modulated graphene monolayer. Phys Rev B 2014;89:081410.
[75] Novoselov KS, Jiang D, Schedin F, et al. Two-dimensional atomic crystals. Proc Natl Acad Sci USA 2005;102:10451–3.
[76] S. Dai, Fei Z, Ma Q, et al. Tunable phonon polaritons in atomically thin Van der Waals crystals of boron nitride. Science 2014;343:1125–30.
[77] Kumar A, Low T, Fung KH, Avouris P, Fang NX. Tunable light-matter interaction and the role of hyperbolicity in graphene-hBN system. Nano Lett 2015;15:3172–80.
[78] Yoxall E, Schnell M, Nikitin AY, et al. Direct observation of ultraslow hyperbolic polariton propagation with negative phase velocity. Nat Photon 2015;9:674–9.
[79] Giles AJ, Dai S, Vurgaftman I, et al. Ultralow-loss polaritons in isotopically pure boron nitride. Nat Mater 2018;17:134–9.
[80] Shapoval OV, Gomez-Diaz JS, Perruisseau-Carrier J, Mosig JR, Nosich AI. Integral equation analysis of plane wave scattering by coplanar graphene-strip gratings in the THz range. IEEE Trans Terahertz Sci Technol 2013;3:666–74.
[81] Kaipa CSR, Yakovlev AB, Hanson GW, Padooru YR, Medina F, Mesa F. Enhanced transmission with a graphene-dielectric microstructure at low-terahertz frequencies. Phys Rev B 2012;85:245407.
[82] Morita A. Semiconducting black phosphorus. Appl Phys A 1986;39:227–42.
[83] Li L, Yu Y, Ye GJ, et al. Black phosphorus field-effect transistors. Nat Nanotechnol 2014;9:372–7.
[84] Koenig SP, Doganov RA, Schmidt H, Neto AH, Oezyilmaz B. Electric field effect in ultrathin black phosphorus. Appl Phys Lett 2014;104:103106.
[85] Correas-Serrano D, Gomez-Diaz JS, Alvarez-Melcon A, Alù A. Black phosphorus plasmonics: anisotropic elliptical propagation and nonlocality-induced canalization. J Opt 2016;18:104006.
[86] Low T, Rodin AS, Carvalho A, et al. Tunable optical properties of multilayers black phosphorus. Phys Rev B 2014;90:075434.
[87] Lumerical Solutions [online]. Available at http://www.lumerical.com/tcad-products/fdtd/. Accessed 05/04/2018.